Materials Today Physics 30 (2023) 100947

Contents lists available at ScienceDirect

Materials Today Physics

journal homepage: www.journals.elsevier.com/materials-today-physics

Tunable plasticity in functionalized honeycomb synaptic memristor for neurocomputing

Qin Gao [a,b], Jiangshun Huang [a], Juan Gao [a], Xueli Geng [a], Yuhang Ji [a], Haoze Li [a], Guoxing Wang [a], Bo Liang [a], Mei Wang [a], Zhisong Xiao [a], Ying Zhu [b], Paul K. Chu [c], Anping Huang [a,*]

[a] School of Physics, Beihang University, Beijing, 100191, China
[b] Key Laboratory of Bio-Inspired Smart Interfacial Science and Technology of Ministry of Education, School of Chemistry, Beihang University, Beijing, 100191, China
[c] Department of Physics, Department of Materials Science and Engineering, And Department of Biomedical Engineering, City University of Hong Kong, Tat Chee Avenue, Kowloon, Hong Kong, China

ARTICLE INFO

Keywords:
Synaptic memristor
Quantum dots
Tunable plasticity
Neuromorphic computing

ABSTRACT

Tunable plasticity is one of the important features in synapses and plays a key role in neuromorphic computing (neurocomputing, NC), maintaining a stable pulse neural network environment, and realizing accurate image recognition. Herein, a functionalized honeycomb-like synaptic memristor (HLSM) composed of porous silicon oxide incorporated with MoS_2 quantum dots (QDs) is fabricated and the synaptic properties such as paired-pulse facilitation (PPF), post-tetanic potentiation (PTP), learning-forgetting behavior, and spike-timing-dependent plasticity (STDP) are simulated. A critical characteristic of short/long-term plasticity (SLTP) is observed from the HLSM device for the sliding frequency threshold between 200 μs and 10 ms and tunable synaptic plasticity is realized without gate voltage regulation. An artificial neural network (ANN) based on the potentiation/depression characteristics is designed theoretically and the recognition rate is observed to increase from 54.2% to 91.8% by simply adjusting the input frequency. The underlying mechanism of the tunable synaptic plasticity is proposed and discussed by taking advantage of the honeycomb structure on fluid buffering and acceleration. The results and theoretical understanding are expected to accelerate the application in NC to image recognition.

1. Introduction

Owing to data bandwidth constraints and growing computing demand, mimicking the neurobiological architecture is one of the promising methods for NC [1,2]. Synaptic plasticity is a key factor in the neurobiological architecture and simulation is an important step to design efficient artificial NC systems [3–5]. The tunable plasticity which is related to the interactions between receptor proteins and external stimuli in synapses constitutes an important link that affects the dynamic ion migration process. By adopting neurobiological principles, plasticity regulation is important to the temporal dynamics of biological neural networks. However, in traditional neuromorphic devices, both the long-term plasticity (LTP) and short-term plasticity (STP) of synapses are usually simulated by homologous physical mechanisms in the same region of the device, resulting in mutual exclusion and non-coexistence of two kinds of plasticity.

For this reason, multi-terminal devices have attracted a lot of attention lately due to the tunable and resistive switching dynamics on various external stimulus scales. The methods for plasticity regulation mainly include gate-voltage regulation, multi-gate regulation and light regulation. Nomura et al. have proposed a 2D-SnO_2 memtransistor with dynamically tunable analog switching by regulating the gate bias with good linearity to achieve an improved conductance change ratio for high recognition accuracy 92.25% [6]. Additional interneurons are used to regulate the synaptic plasticity to simulate heterosynaptic plasticity which can stabilize the activity of postsynaptic neurons and avoid excessive excitation and suppression. A 2D WSe_2-based memtransistor has been constructed to mimic both the homosynaptic and heterosynaptic plasticity by optimizing two input conditions (V_{DS} and V_{GS}) and improving the resistance state and linearity of the device [7]. This multi-gate tunable method offers a versatile reconfigurability of excitatory and inhibitory plasticity which is beneficial to the development of

* Corresponding author.
E-mail address: aphuang@buaa.edu.cn (A. Huang).

https://doi.org/10.1016/j.mtphys.2022.100947
Received 15 September 2022; Received in revised form 19 November 2022; Accepted 5 December 2022
Available online 7 December 2022

NC systems. Moreover, an optical signal can act as another modulatory terminal for the quasi-plane $MoSe_2/Bi_2Se_3$ heterostructure to attain heterosynaptic plasticity [8]. Although some progress has been made to plasticity and its regulation, it is still difficult to accomplish tunable synaptic plasticity but needs to be integrated into future NC devices [9].

Nature inspires the design and construction of structures for mutual transformation of synaptic plasticity. In this work, a functionalized honeycomb synaptic memristor consisting of QDs@SiO_x films is designed and fabricated to achieve biomimetic synapses with tunable plasticity. The dynamic behavior of STP and LTP in biological synapses is simulated and the mechanism responsible for the tunable synaptic plasticity is proposed and discussed. Moreover, simulation is performed on synaptic pattern recognition and the synaptic device comprising QDs@SiO_x films exhibits a high fault tolerant capability. The results reveal the important role in maintaining a stable artificial neural network environment in order to realize accurate image recognition.

2. Results and discussion

The HLSM device consists of two different oxide layers as shown in Fig. 1(a) and the high-resolution transmission electron microscopy (HR-TEM) image of the Pt/$PLiCoO_2$/QDs@SiO_x/Si memristor prepared with a focused ion beam (FIB) is depicted in Fig. 1(b). The properties are determined according to the direct current (DC) mode using the Keithley 4200-SCS. The devices are analyzed by scanning the voltage from 5 V to −5 V using a voltage step and current compliance (I_{cc}) of ±0.01 V and 1 mA, respectively, as shown in Fig. 1(c). The currents of the QDs@SiO_x-based memristor change slowly but continuously from both the positive and negative directions thus forming the basis of synaptic conductance control. The high resistive state (HRS) and low resistive state (LRS) for 128 switching cycles disclose the on-off ratio is close to 10^4 for the QDs@SiO_x-based memristor as shown in Fig. 1(d). The retention time of HRS and LRS measured at a small reading voltage of 0.1 V is 10^5 s as shown in Fig. 1(e), implying that the memristor delivers good memory performance which can emulate learning rules. In addition, 5-level states between HRS and LRS were measured and the retention characteristics over 10^3 s with a time step of 5 s and the read voltage is 0.1 V after a specific voltage sweep from 1 V to 5 V, respectively, as shown in Fig. S1. The device-to-device variation is analyzed by scanning the voltage from 5 V to −5 V using a voltage step of ±0.01 V and I_{cc} of 1 mA, respectively, as shown in Fig. S2. The data of 23 devices from *I–V* curves were compared and the characteristics of the *I–V* curves are similar to Fig. 1(c). The HRS and LRS values with 23 devices were statistically investigated, the HRS range is from 10^6 to10^{10} Ω and the LRS range is from 10^3 to10^6 Ω, respectively. The fitting parameter R^2 is 0.99 by Gaussian fitting which implies that the similarity among the devices has been observed, as shown in Fig. 1(f). The structure with no QDs is presented in Fig. S3(a) and the current rises abruptly for 0.74 V–1.26 V. The energy consumption and corresponding electric field of the device are 178.15 nJ and ~4.11×10^6 V/m, respectively, in the first cycle [Fig. S3 (b)]. The device changes from being a digital to analog memristor due to the presence of MoS_2-QDs.

The mechanism of the SiO_x and QDs@SiO_x devices is investigated. In the positive voltage scans from 0 V to 0.34 V, the fitted results in HRS with a slope (S) of 0.38 correspond to thermionic emission conduction as shown in Fig. S3(c) and the conduction mechanisms are described by the following equations:

$$J = \frac{9}{8}\varepsilon\mu\frac{V^2}{d^3}, \tag{1}$$

Under low voltage region, the injected carrier density induced by voltage is low and the device follows Ohm's law [10]. The injected carrier density becomes higher with the voltage increase, where the mechanism of device turned from Ohm's law to trap limited SCLC. The results indicate that metal cations from dissolution of $LiCoO_2$ cause thermionic Schottky emission that can be described by the following equation [10,11].

$$\ln I \propto \sqrt{\frac{q^3}{4\pi\varepsilon d}}KT \times \sqrt{V}, \tag{2}$$

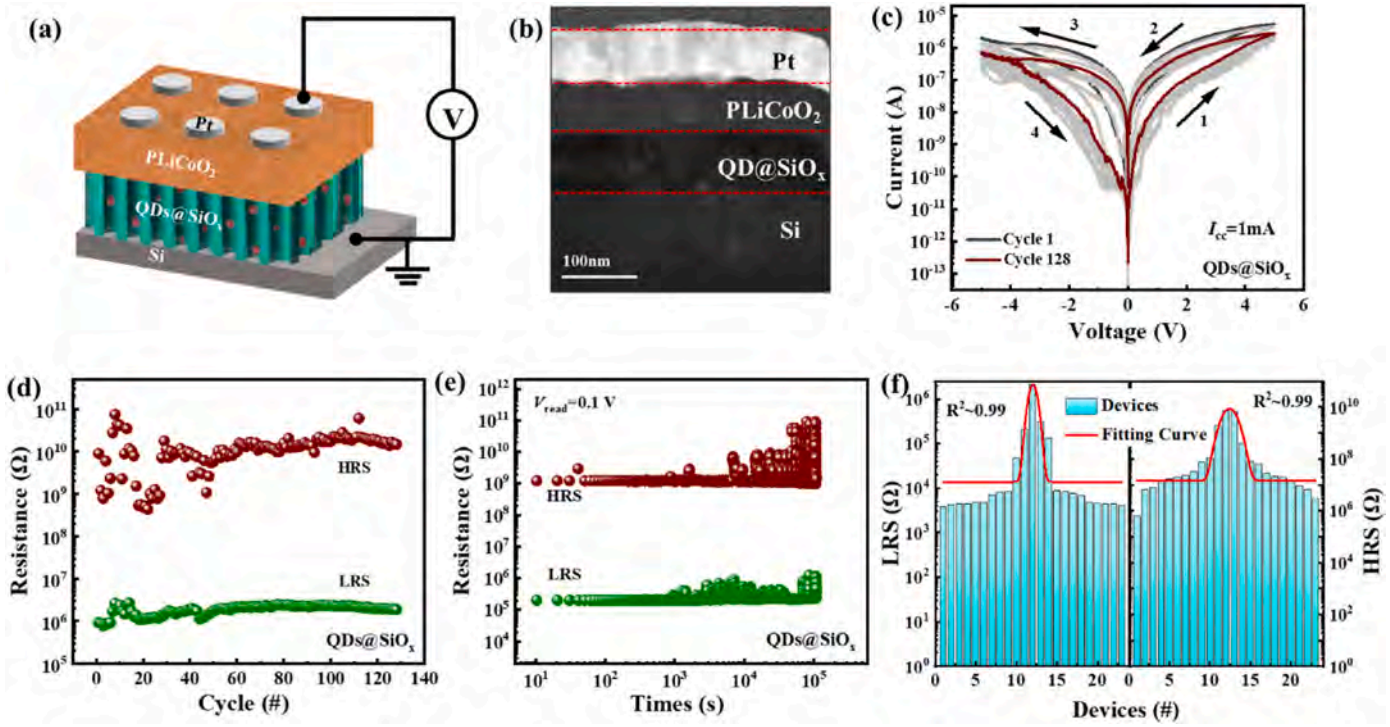

Fig. 1. Structure and memristive properties of the Pt/$PLiCoO_2$/QDs@SiO_x/Si memristor: (a) Schematic diagram of the Pt/$PLiCoO_2$/QDs@SiO_x/Si stack; (b) HR-TEM image of the Pt/$PLiCoO_2$/QDs@SiO_x/Si stack; (c) *I–V* curves for 128 sweeping cycles; (d) Durability evaluation; (e) Retention test; (f) The statistics data of the HRS and LRS values with 23 devices by the sweeping voltage from 5 V to −5 V. The fitting parameter R^2 is 0.99 based on the Gaussian distribution.

where q, ε, d, K, J, T and μ are the electronic charge, dielectric constant, film thickness, Boltzmann's constant, current density, absolute temperature, and carrier mobility, respectively. The I–V curves of thermionic emission conduction are replotted as $\ln I$–$V^{1/2}$ in Fig. S3(d) and the carrier injection barrier causes a low injection efficiency resulting in thermionic emission. Meanwhile, the fitted results for the transition from HRS to LRS show slopes (S2, S3 and S4) of 1.05, 1.79, and 1.04 corresponding to ohmic conduction ($I \propto V$), space-charge-limited current (SCLC, $I \propto V^2$) and ohmic conduction ($I \propto V$), respectively [12]. It is replotted as a linear I–V relationship in Figs. S3(e) and S3(f). Both the Ohmic conduction behavior in the LRS and sharp current increases in the set process are typical features of the conductive filament mode in the resistive switching mechanism. In the QDs@SiO_x device, the double-logarithmic plot shows the fitted conduction mechanism for positive voltage sweeps as shown in Fig. S4(a). Compared to mere Ohmic conduction in LRS (S5~1.05), HRS shows a complicated behavior with three parts dominated by SCLC ($I \propto V^2$, S2~2.05), trap-filled limited current ($I \propto V^{\alpha}$, S3~ 4.73, $\alpha > 2$), as well as thermally generated free carriers (S4 ~1.62) indicative of trap-controlled charge transportation in the HRS. It should be noted that the current increases smoothly and stepwise from the HRS to LRS and there is no sharp increase in the set process due to the QDs with lithium ions. The linear I–V relationship is replotted in Figs. S4(b)–(d).

According to the I–V curve, the vertical porous device maintains the LRS and it is difficult to change to the HRS by increasing the number of cycles. Owing to the large specific surface area of porous silicon oxide and large electric field in the vicinity, ions are more easily bound to the deep vertical porous silica wells because of the confinement effect. Therefore, the vertical porous structure has good storage characteristics and ions can bind to the porous silica layer during repeated cycling. In fact, the tortuosity porous structure shows improved ion transport and device properties [13,14]. According to the honeycomb structure in nature, the device structure can be optimized to show new electrical properties in NC. QDs are suitable materials to embellish the structure because of the excellent physical characteristics. Introducing quantum dots into the vertical porous structure can change the field intensity distribution in the porous structure as shown in Fig. 3(h). The I–V characteristics for different voltage scanning programs are monitored. As the programmed voltage increases, the hysteresis loop becomes large as shown in Fig. 2(a) because the stronger external electric field drives more lithium ions out of $LiCoO_2$ and expedites the reactions between SiO_x and MoS_2 [9,15–17]. Consecutive positive and negative voltage scans are applied and the V–t and I–t curves are displayed in Fig. 2(b) and (c) which show cumulative memory effects with the increasing/decreasing voltages.

Based on the memristor characteristics in the DC test, plasticity simulation is performed on the corresponding functions of biological synaptic systems. A biological synapse which connects the pre- and post-synaptic neuron is a two-terminal device and the stress response of living organisms is related to the strength and frequency of external stimuli. To study the strength and frequency sensitivity, a series of voltage pulses with different numbers, amplitudes, widths, and intervals are applied. The synaptic weight represents the strength of the signal connection

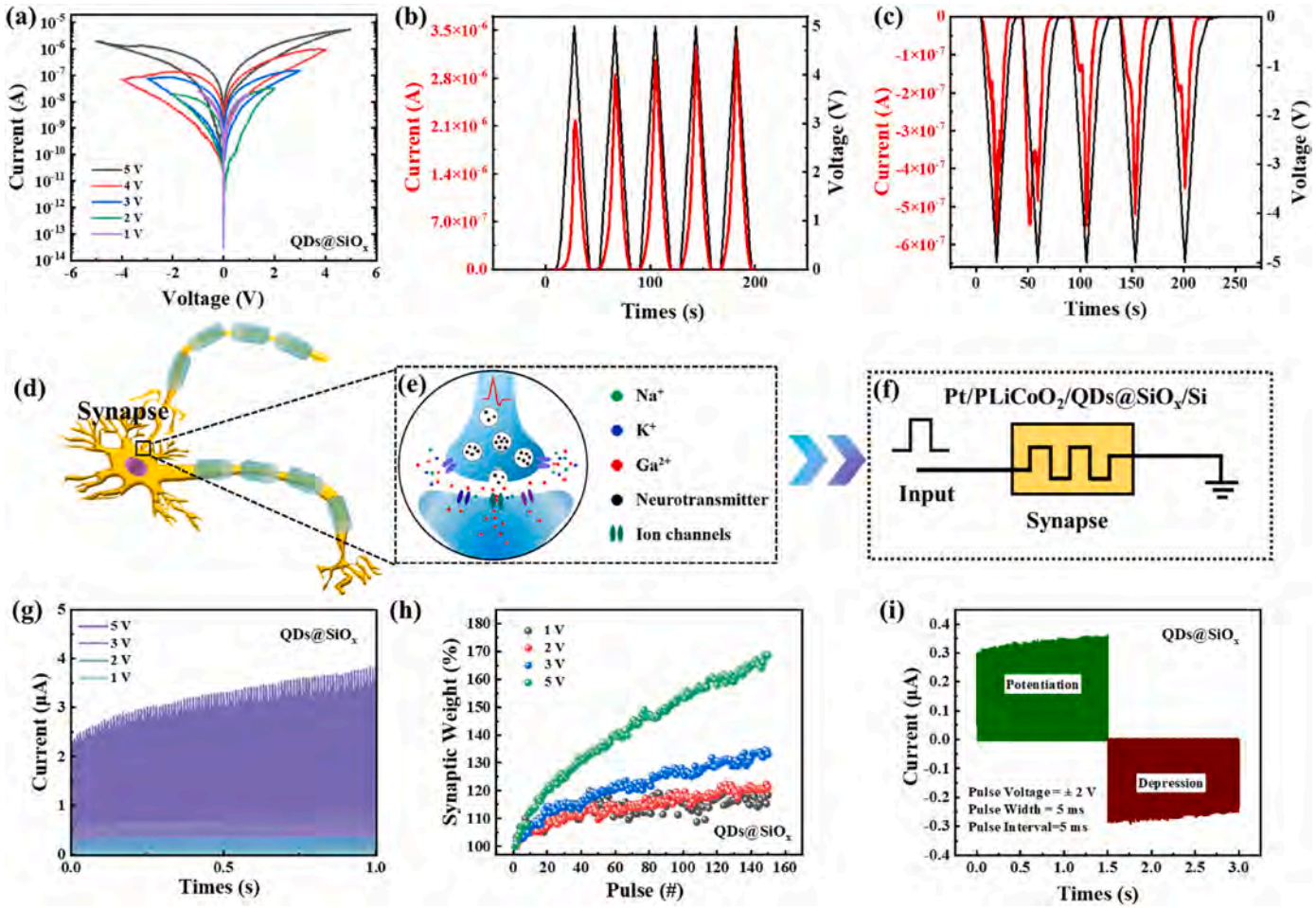

Fig. 2. Device properties: (a) I–V curves for different voltage sweeps; (b) Positive cumulative effects; (c) Negative cumulative effects; (d) Diagram of interconnected neurons; (e) Synapse; (f) Full memristor-based artificial circuit; (g) Different amplitude pulse trains and (h) Larger pulse amplitude causing obvious variation in the synaptic weight; (i) Device conductivity increasing or decreasing by consecutive potentiating or depressing pulses.

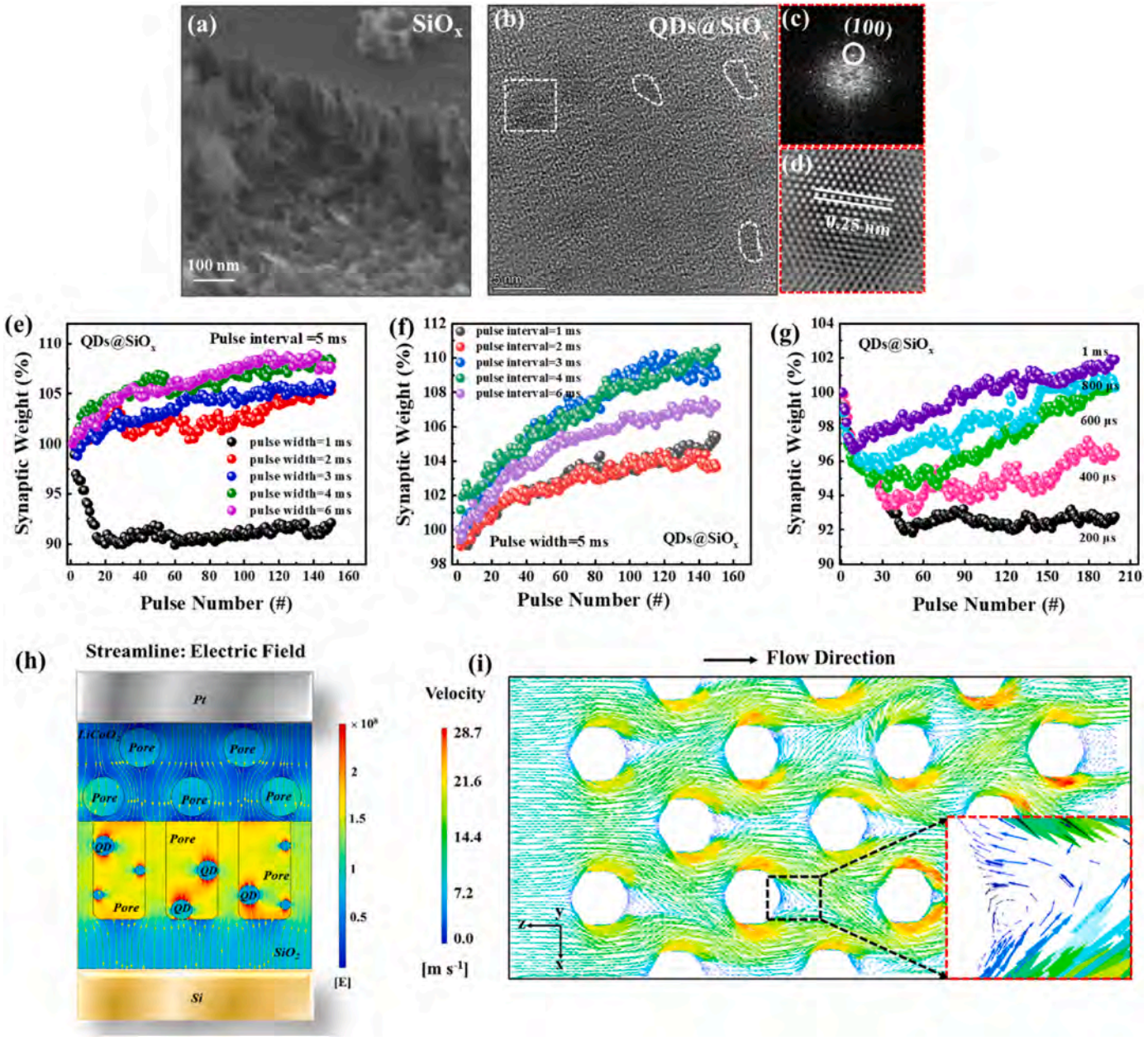

Fig. 3. Synaptic plasticity study: (a) SEM image of SiO_x; (b) HR-TEM image of pristine MoS_2-QDs@SiO_x; (c) FFT image of the white square region in (b); (d) IFFT image of (b); (e) Synaptic plasticity for different pulse widths; (f) Synaptic plasticity for different pulse intervals; (g) Synaptic plasticity for different pulse periods; (h) Electric field simulation of the QDs@SiO_x-based memristor by the COMSOL Multiphysics software; (i) Simulation of the fluid field effect in the honeycomb structure by Ansys software and the red box area in the lower right corner is an enlarged view of the black box.

between two neurons and the change in the electrical conductivity reflects indirectly the synaptic weight of the device. The factors that affect the conductance of the device are related to the current and voltage as shown in the following equation:

$$G = I/U. \tag{3}$$

Fig. 2(d) depicts the interconnected neurons and the connections between neurons are called synapses as shown by the black boxes. Fig. 2 (e) presents the magnified black box in Fig. 2(d) and (f) shows the full memristor-based artificial circuit. The top and bottom electrodes can be regarded as the pre- and post-synaptic neurons, respectively and the $PLiCoO_2$ layer and QDs@SiO_x layer are the pre- and post-synaptic membranes, respectively. Fig. 2(g) shows the influence of strength on the device conductance. The pulse width and interval are 5 ms and 5 ms, respectively. The pulse amplitude is modulated to monitor the conductance for the pulse response as shown in Fig. 2(g) and (h). The conductance of the system changes slightly during the pulse when the absolute voltage is lower than 3 V. When the voltage is larger than 3 V, the synaptic weight changes obviously as shown in Fig. 2(h), indicating that the synapse weight can be regulated by the strength stimuli. The change in the synaptic weight is described by the following equation:

$$W\% = (G_n / G_0) \times 100\%, \tag{4}$$

where G_0 is the conductance in the initial state and G_n (n = 1,2,3, …150) is the corresponding conductance after stimulation. Current regulation is considered to be related to migration of lithium ions in the lithium cobalt oxide layer and QDs@SiO_x layer together with the electrochemical reaction process between silicon oxide [16] and MoS_2-QDs [15,18] as shown in the following:

$$LiCoO_2 - e^- \leftrightarrow Li_xCoO_2 + Li^+, \quad (5)$$

$$SiO_2 + Li^+ + e^- \leftrightarrow Li_ySiO_2, \quad (6)$$

$$Li^+ + MoS_2 \leftrightarrow Li_zMoS_2. \quad (7)$$

As the frequency of the stimulus pulse increases, lithium ions are released from the $PLiCoO_2$ layer to become Li_xCoO_2 and the $PLiCoO_2$ layer changes gradually from an insulator to a semiconductor or even conductor. Under the electric field, lithium ions migrate along the porous channels and react with SiO_x to generate Li_ySiO_2. By continuous stimulation with positive voltage pulses, the concentration of lithium ions increases gradually and electrons in the embedded Li are transferred to the 4*d* orbit of Mo and therefore, Mo^{4+} is converted into Mo^{3+} due to the electrons [19,20]. The concentration of Mo^{3+} in MoS_2 increases gradually and the semiconducting MoS_2 morphs gradually into the metallic state, so that the conductivity increases gradually. The conductance is modified under 150 set pulses (2 V, 5 ms, 5 ms) followed by 150 reset pulses (−2 V, 5 ms, 5 ms) as shown in Fig. 2(i). When a negative voltage pulse is applied, lithium ions are released from the QDs@SiO_x layer and recombine with holes in the Li_yCoO_2 layer. In addition, with decreasing lithium ion concentrations, electrons provided by lithium are separated from the 4*d* orbital of Mo and the metallic phase MoS_2 transforms into a semiconductor, so that the conductivity decreases gradually [21].

The impact of the pulses on conductance modulation is investigated and electrical measurements are carried out by changing the input pulse parameters. Fig. 3(a) reveals that the SiO_x layer has a vertical porous structure and the distribution of the MoS_2-QDs in SiO_x layer is presented in Fig. 3(b). Fig. 3(c) shows the fast Fourier transform (FFT) results of the square region in Fig. 3(b) and the inverse IFFT is displayed in Fig. 3 (d). The HR-TEM images reveal that the MoS_2-QDs have an interplanar spacing of 2.5 Å consistent with the (100) facet. The pulse strength and pulse interval are fixed at 2 V and 5 ms, respectively, while the pulse width is changed. The longer the stimulation, the more intense is sensitization and the higher is the final excitation state as shown in Fig. 3 (e). When the pulse width is 1 ms, the synaptic weight of the device shows temporary attenuation when stimulated by the first 20 pulses exhibiting short-term depression (STD) [22]. By repetitive pulse stimulation, the synaptic weight increases gradually but does not return to the original state. Therefore, the device exhibits long-term depression (LTD) as shown in Fig. S5(a). With a larger pulse width, the synaptic weight increases gradually and the device changes from STD to long-term potentiation (LTP) for pulse widths of 2 ms and 3 ms as shown in Figs. S5(b) and (c), respectively [4]. When the pulse widths are 4 ms and 6 ms, the synaptic device exhibits the LTP behavior as shown in Figs. S5 (d) and (e), respectively [23]. This phenomenon is analogous to the SLTP characteristics in biological synapses which depend on stimuli such as the frequency in the external environment [24].

In order to verify that the SLTP characteristics are more sensitive under frequency stimulation, fixed pulses with a width of 5 ms and amplitude of 2 V are applied, while the pulse interval is varied as shown in Fig. 3(f). Frequency stimulation may cause the change from STD to LTP as shown in Figs. S6(a)–(c). When the pulse intervals are 4 ms and 6 ms, the device has the LTP behavior as shown in Figs. S6(d) and (e). The synaptic plasticity is related to the ratio of the pulse width to pulse interval and the synaptic weight change is the most obvious when the ratio is 1. That is, when the pulse width is close to the pulse interval, continuous signal stimulation is more likely to change the weight and enhance the connection between two neurons. The synaptic plasticity behavior for the same frequency stimulation is explored [Fig. 3(g)]. The pulse strength is 2 V, the pulse durations are 200 μs, 400 μs, 600 μs, 800 μs, and 1 ms, and the corresponding pulse widths are 100 μs, 200 μs, 300 μs, 400 μs, and 500 μs, respectively. The plasticity changes from STD to LTD for pulse periods of 200 μs and 400 μs, respectively, as shown in Figs. S7(a) and (b). When the pulse periods increase, plasticity changes from STD to LTP as illustrated by Figs. S7(c)–(e). The tunable plasticity as a result of environmental change is very attractive to enhancing the stability and operation of neuromorphic chips.

To understand the impact of the inserted QDs and SiO_x layer, the COMSOL Multiphysics software is implemented to simulate the distributions of the electric field and confirm the electrical field concentration in the nanopores and QDs. The electric field intensity is the largest for the heterojunction composed of QDs and porous SiO_x [Fig. 3(h)] [21]. Here, the arrows represent the direction of the electric field and under the electric field, there is a higher density of electric field and this structure has an inhomogeneous distribution of electric field which is beneficial to regulation the ion transport routes and rates. The results further confirm that the porous structure can concentrate the electric field and ions tend to be move along the molybdenum disulfide quantum dots and silicon oxide contact during interfacial migration. In order to better explain the overall effects caused by the random distribution of QDs in porous silicon oxide, the fluid transport effects in the honeycomb structure are simulated using Ansys software as shown in Fig. 3(i). The specific shape distribution of the honeycomb structure forces the fluid inside the plate to change. Hence, the flow velocity and direction of the fluid change constantly [25]. As the flow velocity increases, the fluid and honeycomb point collide to form a jet and local small whirlpools are generated as shown by the red dashed box at the lower right corner in Fig. 3(i). This feature increases the disturbance effect on the structural fluid and imposes a stable storage and control effect [26]. In the HLSM device, QDs perturb the ion transport paths and the properties of the device is similar to those of the honeycomb structure with regard to fluid transport. Fig. S8(a) shows the excitatory postsynaptic current (EPSC) and the rise time is defined as that rising from 10% to 90% (rise time or switching speed) [27]. The switching speed of the device is measured to be 100–400 μs?as shown in Fig. S8(b). The voltage pulse is 5 V, current is about 1.3 μA, and energy consumption is 650 pJ–2.6 nJ. The energy consumption parameters for various synaptic memristors such as oxide, two dimensional materials and perovskite were summarized in Table S1 as the Supporting Information.

According to the operation principles of biosynapses, a model is constructed to analyze the mechanism of the SLTP behavior for different frequency scans [Fig. 4]. In biological nervous systems, the SLTP behavior is caused by diffusion of plasticity-related proteins that are necessary for adjacent synapses, as shown in Fig. 4(a)–(e). [3,28,29] One of the important characteristics of channel proteins is that their structure and functional states can be changed rapidly by physical and chemical factors inside and outside the cells. In signal transmission, Ca^{2+} competes with Na^+ to bind to sites and the membrane barrier function is illustrated in Fig. 4(e). Finally, the signal shows inhibition because by changing the activity of the presynaptic membrane, the excitability of the postsynaptic neuron decreases resulting in inhibition. The presynaptic membrane is depolarized by excitatory transmitters leading to smaller absolute membrane potentials as shown in Fig. 4(b). When the membrane is excited, the amplitude of the potential and release of transmitters are reduced, thus decreasing the excitatory postsynaptic potential, which is regarded as inhibition. Fig. 4(f)-(i) are the schematics of the HLSM synaptic device in the signal transmission process. In the HLSM device, the QDs and SiO_x correspond to the channel proteins in biological synapses and play regulatory roles in the transportation of lithium ions. Frequency stimulation causes depolarization of the $LiCoO_2$ structure in the presynaptic membrane and release of Li^+ diminishes producing a smaller excitatory postsynaptic potential. In other words, the electric field intensity in the porous channel is greater than that of the external electric field due to the built-in electric field. Therefore, the HLSM device shows a transient inhibitory behavior. The SiO_x and QDs competition for the binding sites of Li^+ generates depolarization of the membrane potential and if the change does not exceed the threshold potential of the cell membrane, the device is still in a state of inhibition. The temporal enhancement of conductance is related to STP and it occurs before complete formation of a conductive

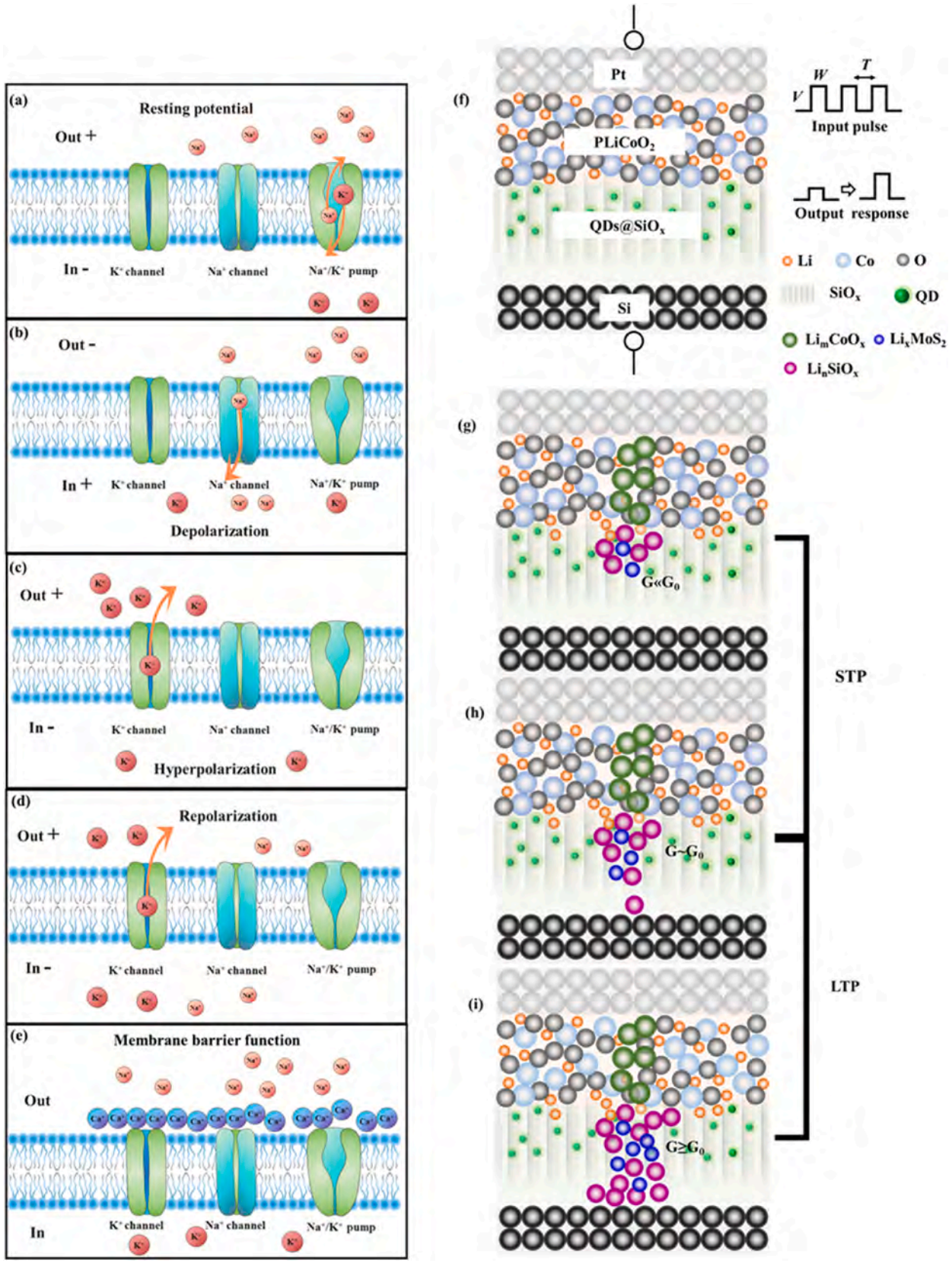

Fig. 4. Model explaining the mechanism of the device: (a)–(e) Schematics of the synapse in the signal transmission process; (f)–(i) Schematics of the QDs@$PSiO_x$ synapse in the signal transmission process; (g) The conductive bridge was not forming and the QDs@$PSiO_x$ synapse working as STP; (h)–(i) Working as LTP after the conductive bridge forming.

bridge. Hence, the decay in conductance can be explained by deformation of an incomplete bridge, that is, G « G_0 as shown in Fig. 4(g). As the number of pulses increases, release of Li^+ increases gradually causing local membrane potential changes. The external electric field increases gradually and the change of the synaptic weights increases gradually, that is, G ~ G_0, as shown in Fig. 4(h). With increasing Li^+ concentrations, the relative potential of the device exceeds the threshold. A robust bridge is formed gradually and the device exhibits the LTP behavior and G ≥ G_0 as shown in Fig. 4(i). In addition, there are a few of oxygen vacancies, which may play a role to reduce the migration barrier, promote the migration of lithium ions and can be helpful to form the conductive channels [30–32].

Multimodal tuning of the synaptic plasticity of paired-pulse facilitation (PPF), post-tetanic potentiation (PTP), learning-forgetting behavior, spike-timing-dependent plasticity (STDP), and learning behavior is verified as shown in Fig. 5. The PPF and PTP are the most well known STP behavior of the device [33] and the STP behavior depends on the time interval between two consecutive pulses and voltage. When the voltage is 5 V and read voltage is 0.5 V, the two consecutive pulse time interval is longer and the current gain is smaller resulting in weaker PPF, which is similar to the biological synaptic behavior. When the time interval between two pulses continues to increase, the change in PPF is not obvious and basically stabilizes at about 29%, as shown in Fig. 5(a). The device corresponds to the double-exponential decay function given by

$$PPF\% = A_0 + A_1\ exp(-\Delta t / \tau_1) + A_2\ exp(-\Delta t / \tau_2), \tag{8}$$

where A_0 is a constant of 29.60 ± 0.09, A_1 and A_2 are the initial facilitation magnitudes of the first and second responses of 3.67 ± 1.01 and 1.49 ± 0, respectively. Δt is the time interval between the pair of stimuli. τ_1 and τ_2 are the characteristic relaxation times of the first and second responses of 11.42 ± 3.28 ms and 0.02 ± 0 ms, respectively.

To explain the PPF and PTP phenomena, the current increase is studied under various stimulation conditions of pulse numbers as shown in Fig. 5(b). The current increase (ΔI) is calculated as $\Delta I = I_n – I_1$, where n is number of following pulses, i. e., n = 1, 2, 3, …, 20, respectively. The value of PPF and PTP for the same spiking intervals is 5 ms and a larger pulse amplitude leads to a large step in the conductance change. The pulse amplitude voltages are 1 V, 3 V, and 5 V, respectively. The long-term memory (LTM) function of the device such as STDP [34,35] is studied and a pair of pulses is applied to the top and bottom electrodes as presynaptic and postsynaptic spikes with V_+/V_- = 5 V/−5 V. The relative timing of the pre- and post-synaptic spikes and time interval (Δt) between them determine the changes in the synaptic weights. According to the asymmetric Hebbian learning rule, when the activity of pre-synaptic neurons precedes that of the post-synaptic neurons, $\Delta t > 0$, otherwise $\Delta t < 0$. In both the pre- and post-synaptic spikes, there is a 3 s interval between V_+ and V_-, which is long enough to ignore the effects of V_+ on V_- according to the decay time of EPSC. The STDP characteristics of the synaptic weight changes are presented in Fig. 5(c) and the fitted curve is described by equation (9):

$$\Delta W = \begin{cases} W_0 + A_+ \exp(-\Delta t/\tau_+) & if\ \Delta t > 0; \\ W_0 + A_- \exp(-\Delta t/\tau_-) & if\ \Delta t < 0, \end{cases} \tag{9}$$

where A and τ are the scale factor and time constant of the STDP function, respectively, and W_0 is a constant representing unassociated synaptic regulation. The pre-spike is sent to the Pt electrode and the post-spike is sent to the Si electrode. Here, τ_+ and τ_- are 15.25 ms and −20.62 ms in the *anti*-Hebbian learning rule, respectively, which match well the time constants in biological synapses.

Learning and memory are the basic functions of the brain and animals can change the behavior and habits to adapt to changes in the outside world by learning [36]. By adjusting the stimulus, the benefits of learning can be judged by the change in the synaptic weight. Here, the learning behavior of the same device is studied by changing the frequency of the input signal for the same time interval Δt of 20 s. The

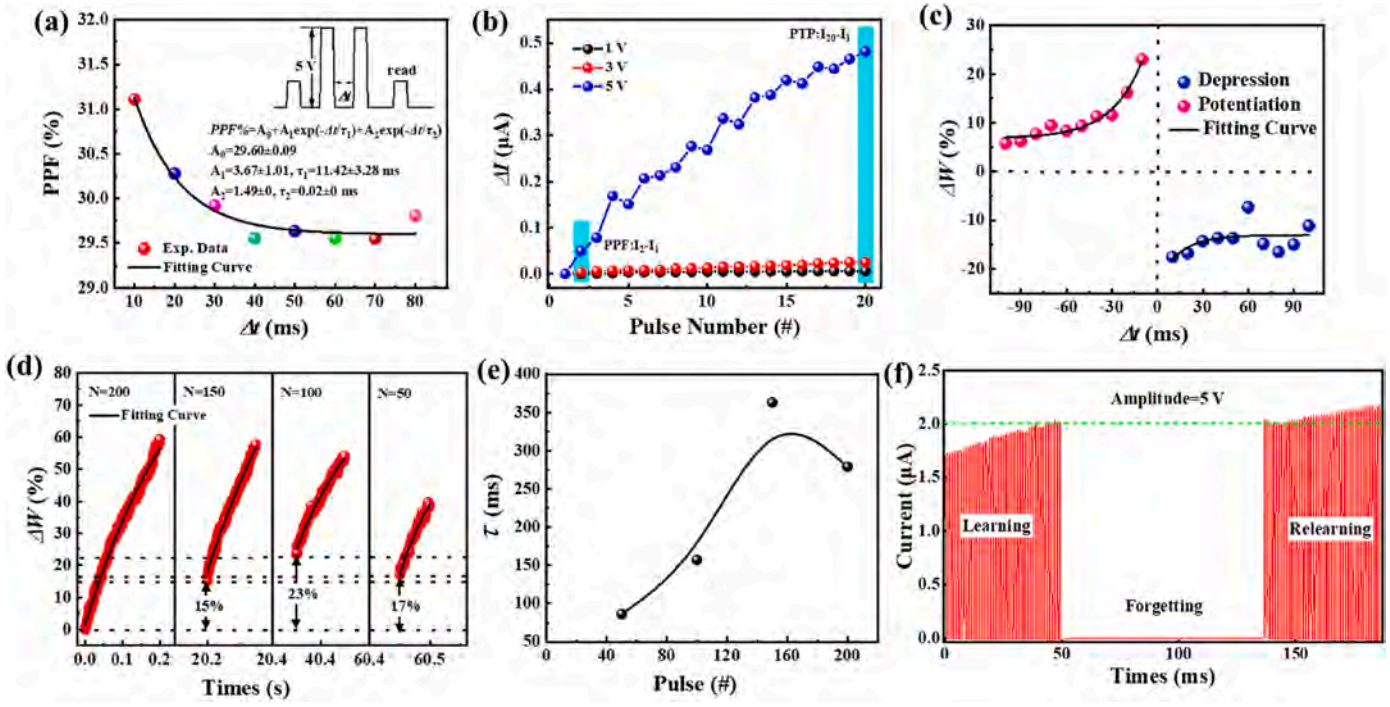

Fig. 5. Multimodal tuning synaptic properties of Pt/PLiCoO$_2$/QDs@SiO$_x$/Si: (a) PPF phenomenon under different Δt conditions; (b) Experimental current changes for twenty consecutive pulses with different programmed pulses of 1 V, 3 V, and 5 V, respectively. The current changes are calculated by $\Delta I = I_N – I_1$, where N = 1, 2, 3, …, 10. The blue boxes show the PPF and PTP phenomena, respectively; (c) STDP behavior of the device; (d) Learning experience stimulated by four repetitive pulses; (e) Variation of the relaxation time constant τ with the number of stimulation pulses, where τ is obtained by fitting the data in (d); (f) Learning-forgetting-relearning phenomenon of the device.

learning and memorization behavior of the device is analyzed indirectly by monitoring the change in the synaptic weight. Fig. 5(d) shows the learning experience for four repetitive pulse stimulation. Two hundred consecutive positive voltage pulses are first applied to the device and the voltage pulses are turned off for 20 s. Afterwards, 150 consecutive positive voltage pulses are applied and the synaptic weight changes by 15%. By applying 100 and 50 consecutive positive voltage pulses, the synaptic weights change by 23% and 17%, respectively. The relaxation process is examined after application of different numbers of stimulation pulses as shown in Fig. 5(e). An exponential equation is used to describe the relaxation process of STP and LTP:

$$M(t) = M_e + (M_0 - M_e)\exp(-t/\tau), \tag{10}$$

where M(t), M_0, and M_e are the memory levels at time t and τ is the

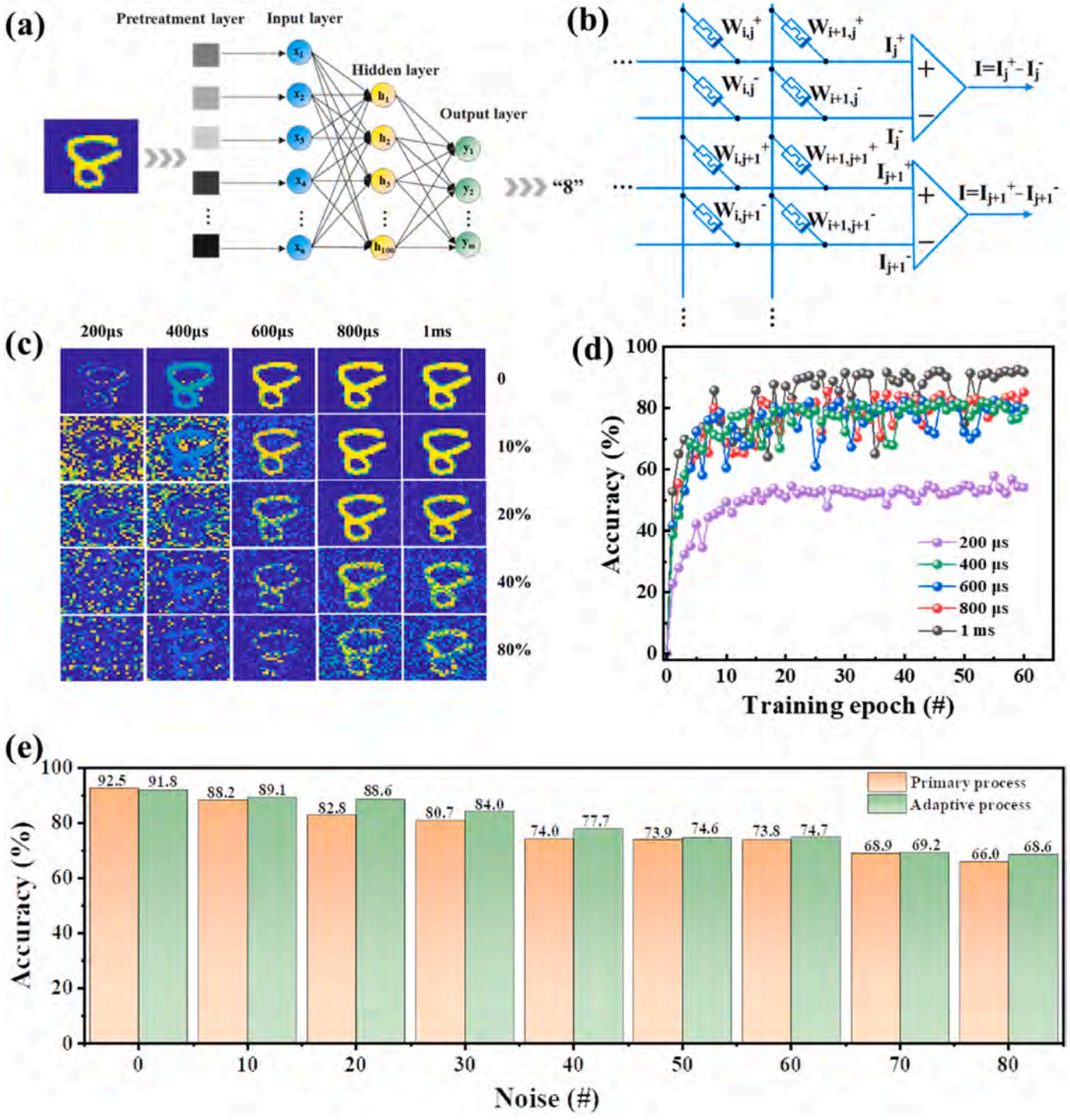

Fig. 6. (a) Schematic illustration of three-layer neural network recognition of handwritten digits with 28 × 28 pixels. In the grayscale image, white (maximum) and black (minimum) correspond to the highest and lowest synaptic weights, respectively; (b) Schematic of the synaptic weight defined as the conductance difference of two equivalent synapses; (c) Comparison of the classification accuracy rates of MNIST digits for five types of experimental dataset with different noise ratios (0–80%) and for five different experimental data sets with 100, 200, 300, 400 and 500 μs SLTP electrical pulse widths; (d) Recognition accuracy of the network for five different experimental datasets training epochs; (e) Recognition accuracy of the network for 1 ms experimental data sets training epochs for different processes.

relaxation time constant which can be used to evaluate the forgetting rate. After repeated and timely learning of the input information, the short-term memory (STM) can become LTM and remain in the human brain for a long time, while τ changes from tens to hundreds of milliseconds [37]. The time interval between the first learning and second learning step is tens of milliseconds and the final state current of the first learning step is almost the same as the initial state current of the second learning step, as shown by the green line in Fig. 5(f). The device shows obvious STM characteristics. Furthermore, repeated training of the device can alter the memory time of the device similar to the learning process in the brain. Because of the tunable plasticity, the device shows that changing stimulation can make the device to transform from STP to LTP, which is very similar to the biosynapse behavior.

To further explore the potential of our synaptic device with tunable plasticity in neuromorphic computing, a handwritten ANN is developed to simulate learning digits from the Modified National Institute of Standards and Technology (MNIST) dataset through the Back-propagation (BP) neural network simulator as shown in Fig. 6. The simulator can recognize an image version utilizing 784 input neurons, 100 hidden neurons, and 10 output neurons, and the adaptive process is studied by adding a pretreatment layer before the input layer as illustrated in Fig. 6(a). The first two layers primarily handle in advance and abstract the input information [38], whereas the last layer makes the decision for the information with features. Fig. 6(b) reveals that a signed weight is mapped to the differential conductance of a pair of memristors. In this manner, all the weights of a kernel are mapped to two conductance rows. The change of conductance in potentiation and depression in Fig. 2(i) is recognized as synaptic weight update to implement pattern recognition. We treat the synaptic behavior from 200 μs to 1 ms as a pretreatment process to adjust the environmental noise. Selecting randomly distributed noise functions, the formula for adding uniformly distributed noise on [−1,1] is:

$$f^{\delta}(X_i) = f(X_i) + \delta(2R_i - 1)f(X), \tag{11}$$

where, $f^{\delta}(X_i)$ is the data with added noise, δ is the relative error level, and R is a random number uniformly distributed on the interval [0, 1]. The uniform random numbers generated in the range of [0, 1] are directly added to each pixel of the image using Matlab software. The 784 input neurons correspond to the input image with a size of 28 × 28 pixels and the 10 output neurons correspond to 10 classes of digits (0–9). In each training epoch, 1000 images are randomly selected from the MNIST training dataset of 60,000 handwritten digit images and sent to the ANN for training. Subsequently, the recognition accuracy of the ANN is estimated using a separate testing dataset of 10,000 images. The recognition accuracy of each epochs is recorded respectively. To demonstrate the fault tolerance capability of the network, different levels of noise are added to the images at different input frequencies as shown in Fig. 6(c). The recognition accuracy of the network in different states improves with time of epoch and evolution of the image during the learning process at various input frequencies. The image recognition accuracy increases from 54.2% (200 μs) to 91.8% (1 ms) as shown in Fig. 6(d). Fig. 6 (e) demonstrates that the accuracy can reach 92.5% without noise for the pretreatment process. This synaptic device is applied to pattern recognition with a strong fault tolerance and the image recognition accuracy is improved by 6% in the presence of 20% noise and moreover, the accuracy is still 68.6% when the noise level is 80%.

3. Conclusion

A biomimetic synaptic device with SLTP properties which can realize tunable plasticity is designed and analyzed. The synaptic device with tunable synaptic plasticity can be applied to image recognition with the accuracy rate of 91.8%. The mechanism of synaptic plasticity regulation is investigated according to the effects of the honeycomb structure on fluid buffering and acceleration. The findings provide insights that are important to the development of high-performance NC systems.

4. Experimental section

4.1. Preparation of Porous SiO_x

The highly doped Si ($\rho < 0.0015$ Ω m and $d = 375 \pm 25$ μm) was processed by electrochemical anodic oxidation in a solution containing 10 vol% HF (≥40%, Sinopharm Chemical Reagent Co., Ltd) in the constant current mode of 60 mA/cm^2 for 60 s at room temperature. After turning off the electric field, the sample was immersed in the electrolyte for 1 h to obtain the uniform porous structure. Porous SiO_x (~100 nm thick, $Ø \sim 10$ nm) was prepared on the porous *p*-type (100) Si substrate by chemical vapor deposition (CVD) at 900 °C for 1 h under an oxygen flow rate of 60 sccm as shown in Fig. S9(a).

4.2. Preparation of QDs@SiO_x/Si

The semiconducting MoS_2-QDs 2–8 nm in size were purchased from Jiangsu Xianfeng Nanomaterial Technology Co., Ltd. Incorporation of the MoS_2-QDs into the porous nanostructure was accomplished by in situ synthesis in the pores. The MoS_2-QDs precursor solution was introduced to the upper surface of the SiO_x/Si substrate to infiltrate the pores as shown in Fig. S9(b). It was followed by evaporation of water and slow heating in an oven to 80 °C as shown in Fig. S9(c) [39].

4.3. Preparation of the Pt/$LiCoO_2$/QDs@SiO_x/Si device

Pt (~80 nm)/$LiCoO_2$ (~60 nm) was prepared on the QDs@SiO_x/Si substrate by magnetron sputtering.

Credit author statement

Qin Gao designed and fabricated the device structure, performed the measurements and analyzed the data, conceived the manuscript concept and wrote the manuscript. Jiangshun Huang finished the pattern recognition part of the manuscript. Anping Huang and Paul K. Chu revised the manuscript and Anping Huang directed the whole work. All the authors discussed the results and commented on the manuscript.

The work is original and has not been published in other journals before the publication of Material Today Physics.

Declaration of competing interest

The authors declare that they have no known competing financial interests or personal relationships that could have appeared to influence the work reported in this paper.

Data availability

Data will be made available on request.

Acknowledgements

This research was supported by the National Natural Science Foundation of China (Grant Nos. 51872010 and 61975005), Foundation of Beijing Academy of Quantum Information Sciences, China (Grant No. Y18G28), and City University of Hong Kong Donation Research Grant, Hong Kong (DON-RMG No. 9229021).

Appendix A. Supplementary data

Supplementary data to this article can be found online at https://doi.org/10.1016/j.mtphys.2022.100947.

References

[1] M.B.N. Graupner, Proc. Natl. Acad. Sci. USA 109 (2012) 3991.
[2] R. Lamprecht, J. LeDoux, Nat. Rev. Neurosci. 5 (2004) 45.
[3] M.H.K.M. Nishiyama, Nature 408 (2000) 584.
[4] D. Muller, S. Hefft, A. Figurov, Neuron (Cambridge, Mass.) 14 (1995) 599.
[5] H. Zhang, T.J. Park, A.N.M.N. Islam, D.S.J. Tran, S. Manna, Q. Wang, S. Mondal, H. Yu, S. Banik, S. Cheng, H. Zhou, S. Gamage, S. Mahapatra, Y. Zhu, Y. Abate, N. Jiang, S.K.R.S. Sankaranarayanan, A. Sengupta, C. Teuscher, S. Ramanathan, Science 375 (2022) 533.
[6] C. Huang, H. Chang, T. Yang, Y. Wang, Y. Chueh, K. Nomura, ACS Appl. Mater. Interfaces 13 (2021) 52822–52832.
[7] G. Ding, B. Yang, R.S. Chen, W.A. Mo, K. Zhou, Y. Liu, G. Shang, Y. Zhai, S.T. Han, Y. Zhou, Small 17 (2021): 2103175.
[8] Y. Wang, J. Yang, Z. Wang, J. Chen, Q. Yang, Z. Lv, Y. Zhou, Y. Zhai, Z. Li, S. Han, Small 15 (2019): 1805431.
[9] V.S. Nguyen, V.H. Mai, P. Auban Senzier, C. Pasquier, K. Wang, M.J. Rozenberg, N. Brun, K. March, F. Jomard, J. Giapintzakis, C.N. Mihailescu, E. Kyriakides, P. Nukala, T. Maroutian, G. Agnus, P. Lecoeur, S. Matzen, P. Aubert, S. Franger, R. Salot, P. Albouy, D. Alamarguy, B. Dkhil, P. Chrétien, O. Schneegans, Small 14 (2018): 1801038.
[10] S. Ge, X. Guan, Y. Wang, C.H. Lin, Y. Cui, Y. Huang, X. Zhang, R. Zhang, X. Yang, T. Wu, Adv. Funct. Mater. 30 (2020): 2002110.
[11] J.S. Han, Q.V. Le, J. Choi, K. Hong, C.W. Moon, T.L. Kim, H. Kim, S.Y. Kim, H. W. Jang, Adv. Funct. Mater. 28 (2018): 1705783.
[12] J. Zhou, W. Li, Y. Chen, Y.H. Lin, M. Yi, J. Li, Y. Qian, Y. Guo, K. Cao, L. Xie, H. Ling, Z. Ren, J. Xu, J. Zhu, S. Yan, W. Huang, Adv. Mater. 33 (2021): 2006201.
[13] Q. Gao, A. Huang, J. Zhang, Y. Ji, J. Zhang, X. Chen, X. Geng, Q. Hu, M. Wang, Z. Xiao, P.K. Chu, NPG Asia Mater. 13 (2021) 1.
[14] Q. Gao, A. Huang, Q. Hu, X. Zhang, Y. Chi, R. Li, Y. Ji, X. Chen, R. Zhao, M. Wang, H. Shi, M. Wang, Y. Cui, Z. Xiao, P.K. Chu, ACS Appl. Mater. Interfaces 11 (2019): 21734.
[15] S. Chen, L. Wang, R. Shao, J. Zou, R. Cai, J. Lin, C. Zhu, J. Zhang, F. Xu, J. Cao, J. Feng, J. Qi, P. Gao, Nano Energy 48 (2018) 560.
[16] I. Bezza, E. Luais, F. Ghamouss, M. Zaghrioui, F. Tran-van, J. Sakai, J. Alloys Compd. 805 (2019) 19.
[17] Q. Hu, R. Li, X. Zhang, Q. Gao, M. Wang, H. Shi, Z. Xiao, P.K. Chu, A. Huang, Sci. Rep. 9 (2019) 5081.
[18] E.J.G. Santos, E. Kaxiras, ACS Nano 7 (2013): 10741.
[19] J.B. Cook, H.S. Kim, Y. Yan, J.S. Ko, S. Robbennolt, B. Dunn, S.H. Tolbert, Adv. Energy Mater. 6 (2016): 1501937.
[20] R. Kappera, D. Voiry, S.E. Yalcin, B. Branch, G. Gupta, A.D. Mohite, M. Chhowalla, Nat. Mater. 13 (2014) 1128.
[21] X. Zhu, D. Li, X. Liang, W.D. Lu, Nat. Mater. 18 (2019) 141.
[22] L. Zhou, S. Yang, G. Ding, J. Yang, Y. Ren, S. Zhang, J. Mao, Y. Yang, Y. Zhou, S. Han, Nano Energy 58 (2019) 293.
[23] T. Ohno, T. Hasegawa, T. Tsuruoka, K. Terabe, J.K. Gimzewski, M. Aono, Nat. Mater. 10 (2011) 591.
[24] A. Rao, P. Plank, A. Wild, W. Maass, Nat. Mach. Intell. 1 (2022).
[25] M.S. Mahdi, A.F. Hasan, Energy Storage (2022) e396.
[26] Y. Zhang, Y. Ni, H. Zhao, S. Hakani, F. Ye, L. DeLong, I. Kimchi, G. Cao, Nature (2022) 1.
[27] L. Min, W. Tian, F. Cao, J. Guo, L. Li, Adv. Mater. 33 (2021): 2101714.
[28] K.L. Magleby, J. Phyaiol. 234 (1973) 327.
[29] J. Tang, F. Yuan, X. Shen, Z. Wang, M. Rao, Y. He, Y. Sun, X. Li, W. Zhang, Y. Li, B. Gao, H. Qian, G. Bi, S. Song, J.J. Yang, H. Wu, Adv. Mater. (2019): 1902761.
[30] V.H. Mai, A. Moradpour, P.A. Senzier, C. Pasquier, K. Wang, M.J. Rozenberg, J. Giapintzakis, C.N. Mihailescu, C.M. Orfanidou, E. Svoukis, A. Breza, C.B. Lioutas, S. Franger, A. Revcolevschi, T. Maroutian, P. Lecoeur, P. Aubert, G. Agnus, R. Salot, P.A. Albouy, R. Weil, D. Alamarguy, K. March, F. Jomard, P. Chrétien, O. Schneegans, Sci. Rep.-UK. 5 (2015) 7761.
[31] F. Wang, L. Mao, X. Qi, L. Xia, H. Xie, J. Mao, Chem. Eng. J. 418 (2021): 129397.
[32] M.S. Munde, D.Z. Gao, A.L. Shluger, J. Phys. Condens. Matter 29 (2017): 245701.
[33] A.S. Sokolov, Y. Jeon, S. Kim, B. Ku, C. Choi, NPG Asia Mater. 11 (2019) 5.
[34] L. Chen, C. Li, T. Huang, H.G. Ahmad, Y. Chen, Phys. Lett. 378 (2014) 2924.
[35] D. Moncada, F. Ballarini, H. Viola, Neural Plast. 2015 (2015): 650780.
[36] V. Erokhin, T. Berzina, P. Camorani, A. Smerieri, D. Vavoulis, J. Feng, M. P. Fontana, BioNanoScience 1 (2011) 24.
[37] J.M.J. Murre, J. Dros, PLoS One 10 (2015): e0120644.
[38] T. Ahmed, M. Tahir, M.X. Low, Y. Ren, S.A. Tawfik, E.L.H. Mayes, S. Kuriakose, S. Nawaz, M.J.S. Spencer, H. Chen, M. Bhaskaran, S. Sriram, S. Walia, Adv. Mater. (2020): 2004207.
[39] N. Massad-Ivanir, S.K. Bhunia, N. Raz, E. Segal, R. Jelinek, NPG Asia Mater. 10 (2018) e463.

Tunable Plasticity in Functionalized Honeycomb Synaptic Memristor for Neurocomputing

Qin Gao, [1&2] Jiangshun Huang, [1] Juan Gao, [1] Xueli Geng, [1] Yuhang Ji,[1]Haoze Li, [1]

Guoxing Wang, [1]Bo Liang,[1] Mei Wang,[1] Zhisong Xiao, [1] Ying Zhu,[2] Paul K. Chu,[3]

Anping Huang[1]*

[1] School of Physics, Beihang University, Beijing 100191, China

[2] Key Laboratory of Bio-Inspired Smart Interfacial Science and Technology of Ministry of Education, School of Chemistry, Beihang University, Beijing 100191, China

[3] Department of Physics, Department of Materials Science and Engineering, and Department of Biomedical Engineering, City University of Hong Kong, Tat Chee Avenue, Kowloon, Hong Kong, China

** Corresponding author: aphuang@buaa.edu.cn (Dr. A. P. Huang); Tel: 86-10-61716876; Fax: 86-10-61716876*

1. Retention characteristics of Pt/PLiCoO$_2$/SiO$_x$/Si structure with 5-level resistance states

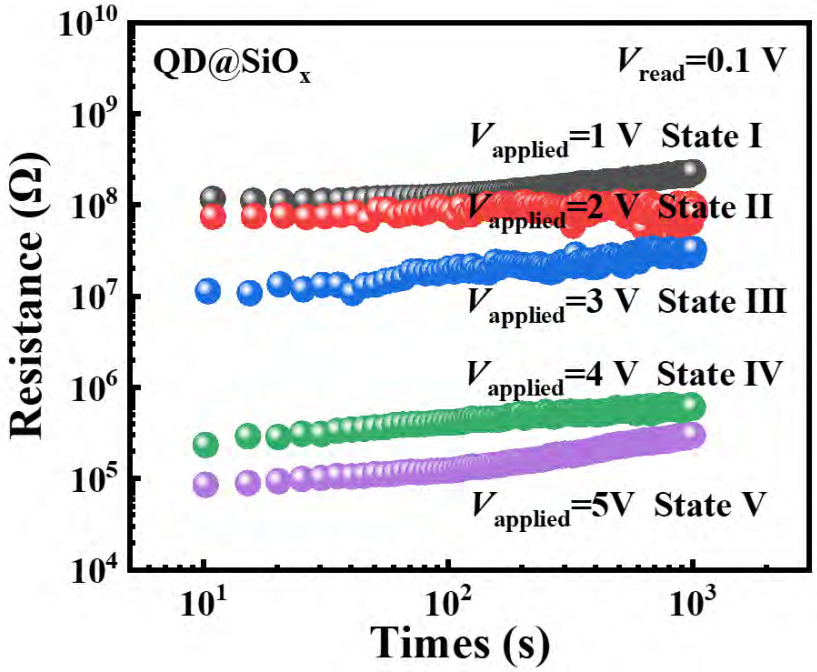

Figure S1. Retention characteristics over 10^3 seconds with a time step of 5 s and the read voltage is 0.1 V after a specific voltage sweep from 1 V to 5 V, respectively.

2. The *I-V* characteristics of device-to-device variation

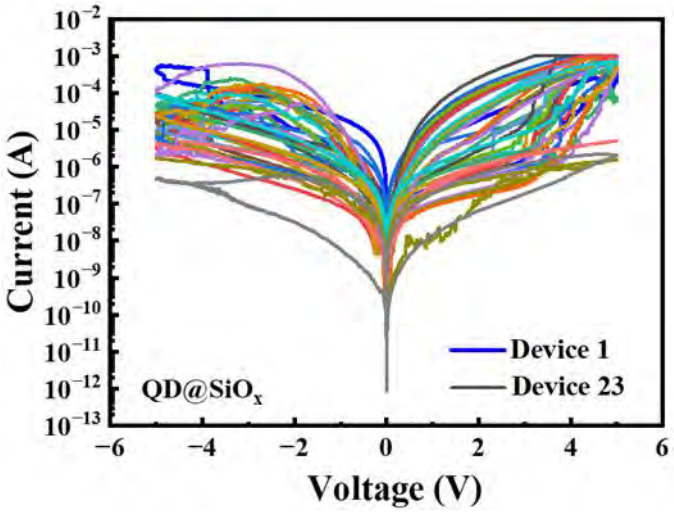

Figure S2. The device-to-device variation is analyzed by scanning the voltage from 5 V to -5 V using a voltage step and I_{cc} of ±0.01 V and 1 mA. The data of 23 devices from *I-V* curves were compared and analyzed. The characteristics of the *I-V* curves are similar to Figure 1(c).

3. Electrical analysis of Pt/PLiCoO$_2$/SiO$_x$/Si

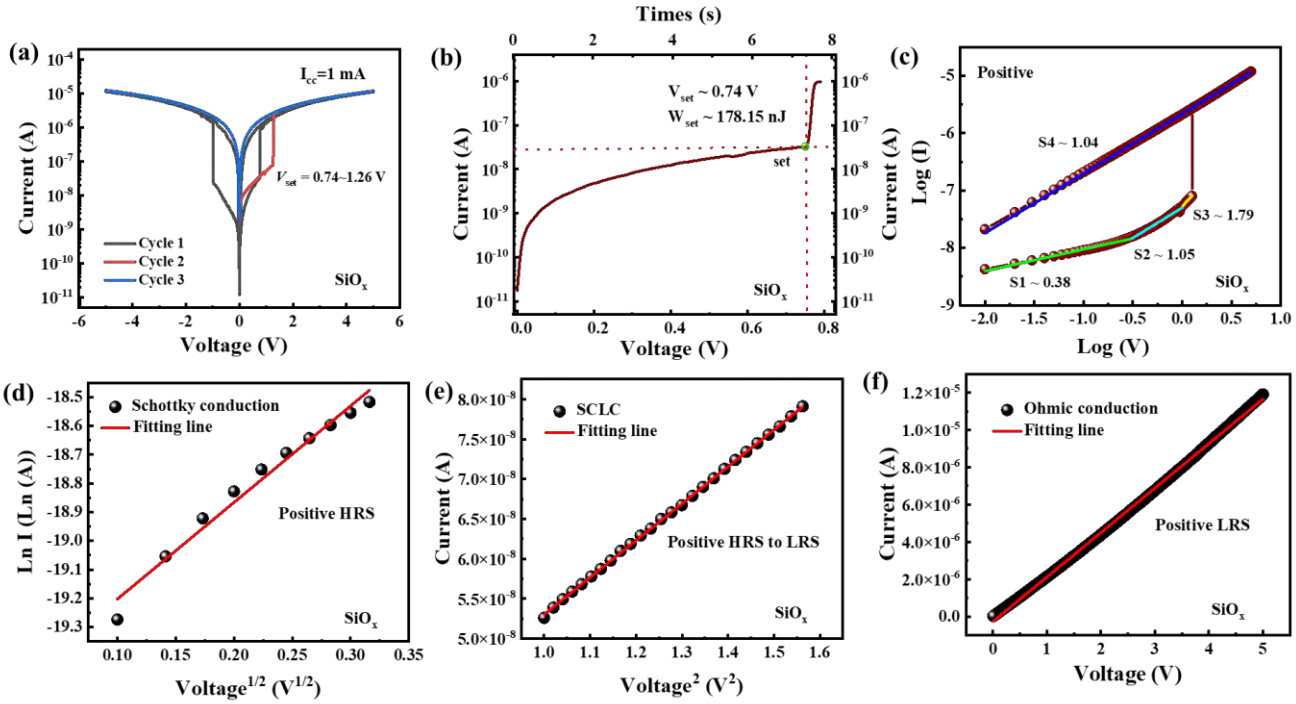

Figure S3. (a) *I-V* curve of SiO$_x$; (b) *I-V* and *I-t* curve; (c) *Log I - Log V* with fitted conduction mechanism for the positive voltage sweep; (d) *lnI-V*$^{1/2}$ plots in HRS for positive voltage sweeps; (e) *I-V*^{2} plots from the HRS to LRS for positive voltage sweeps; (f) *I-V* plots in the LRS for positive voltage sweeps. The straight lines are linear fits.

4. The mechanism analysis of Pt/PLiCoO$_2$/QDs@SiO$_x$/Si

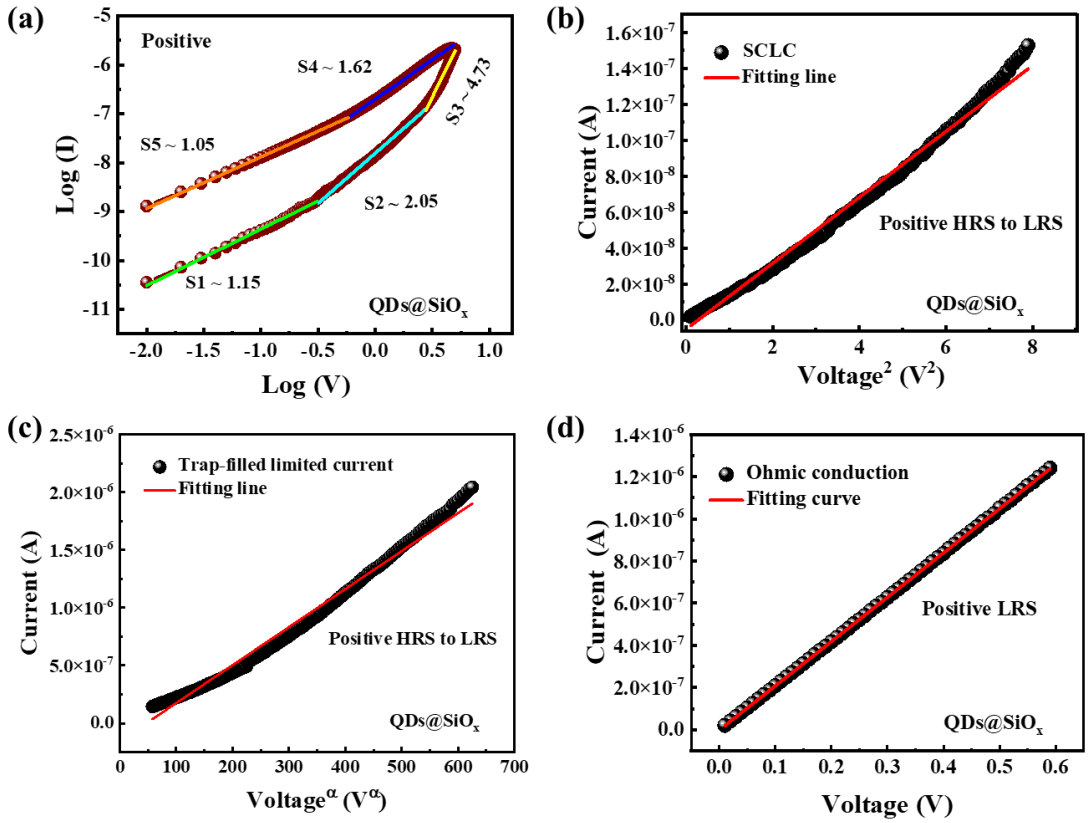

Figure S4. (a) *Log I - Log V* with fitted conduction mechanism for the positive voltage sweep (b) I-V^2 plots from the HRS to LRS for positive voltage sweeps; (c) I-V^α plots from the HRS to LRS for positive voltage sweeps; (d) I-V plots in the LRS for positive voltage sweeps. The straight lines are linear fits.

5. Synaptic plasticity of Pt/PLiCoO$_2$/QDs@SiO$_x$/Si for different pulse widths

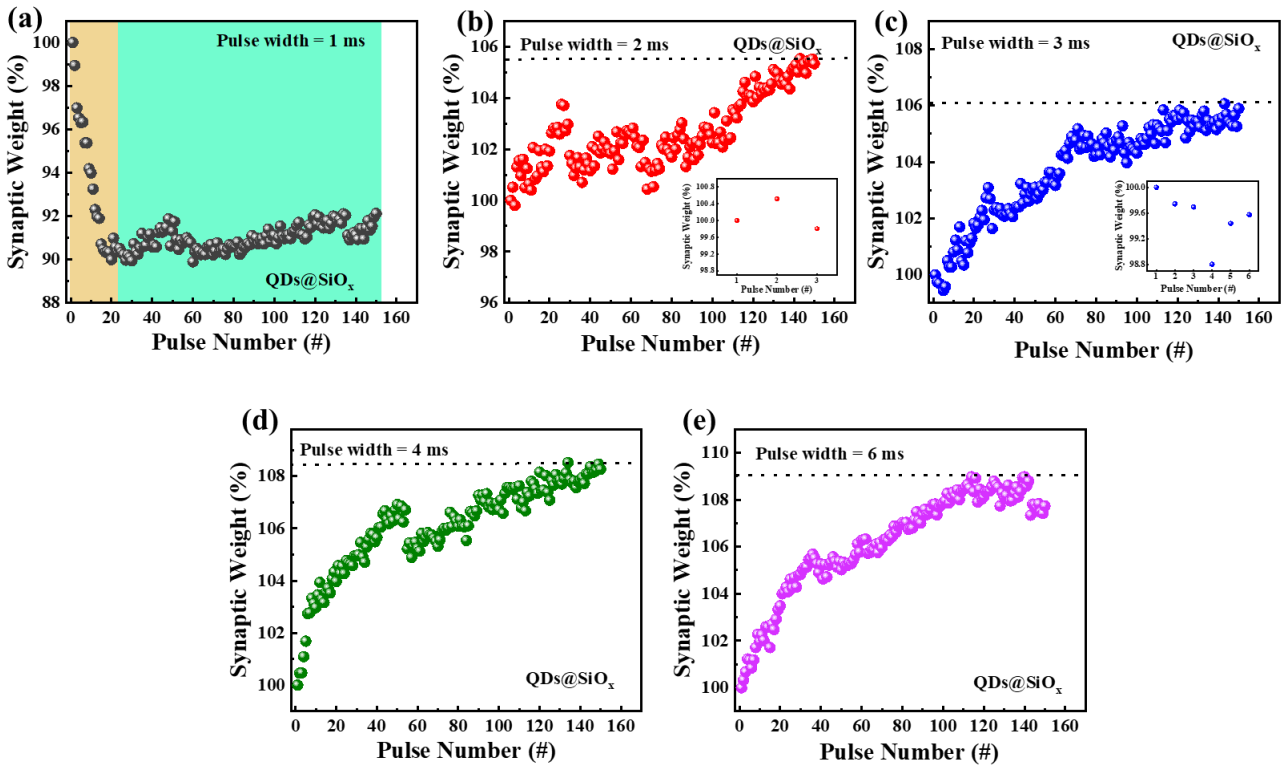

Figure S5. Synaptic plasticity for different pulse widths: (a) 1 ms, (b) 2 ms, (c) 3 ms, (d) 4 ms, and (e) 6 ms.

6. Synaptic plasticity of Pt/PLiCoO$_2$/QDs@SiO$_x$/Si for different pulse intervals

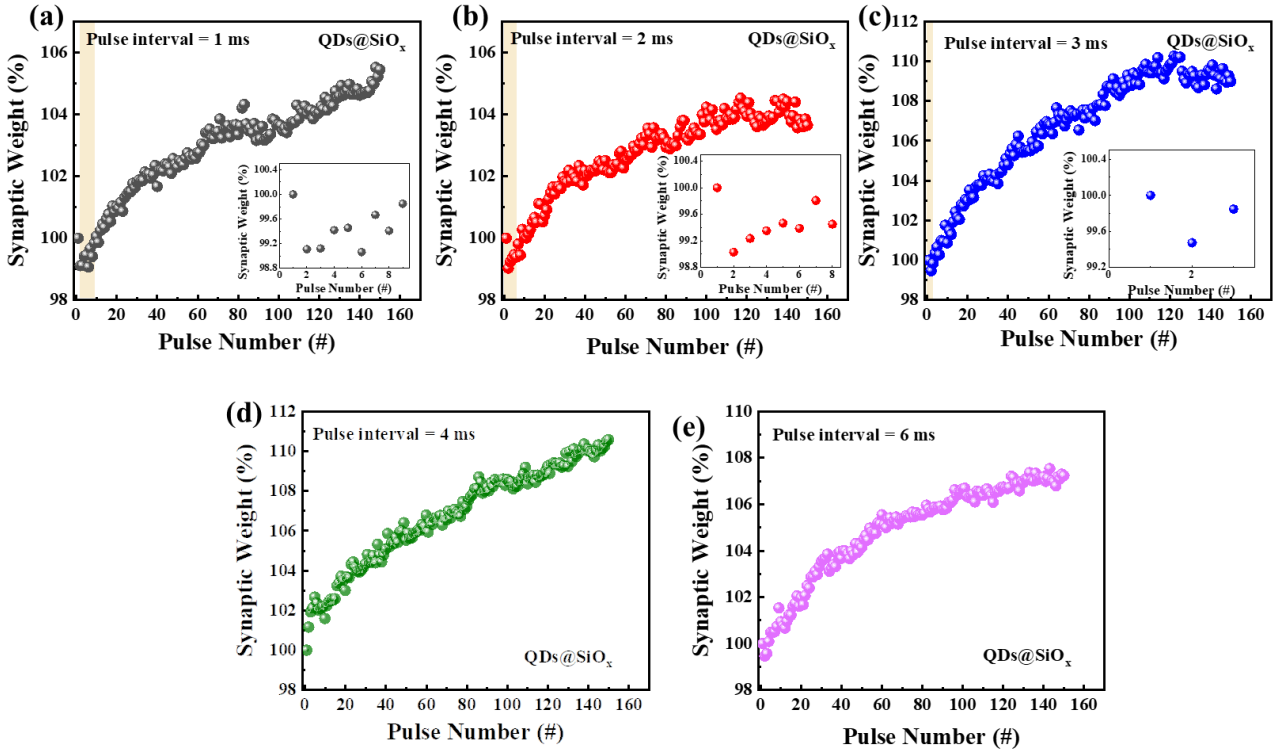

Figure S6. Synaptic weights for different pulse intervals: (a) 1 ms, (b) 2 ms, (c) 3 ms, (d) 4 ms, and (e) 6 ms.

7. Synaptic plasticity of Pt/PLiCoO$_2$/QDs@SiO$_x$/Si for different pulse widths

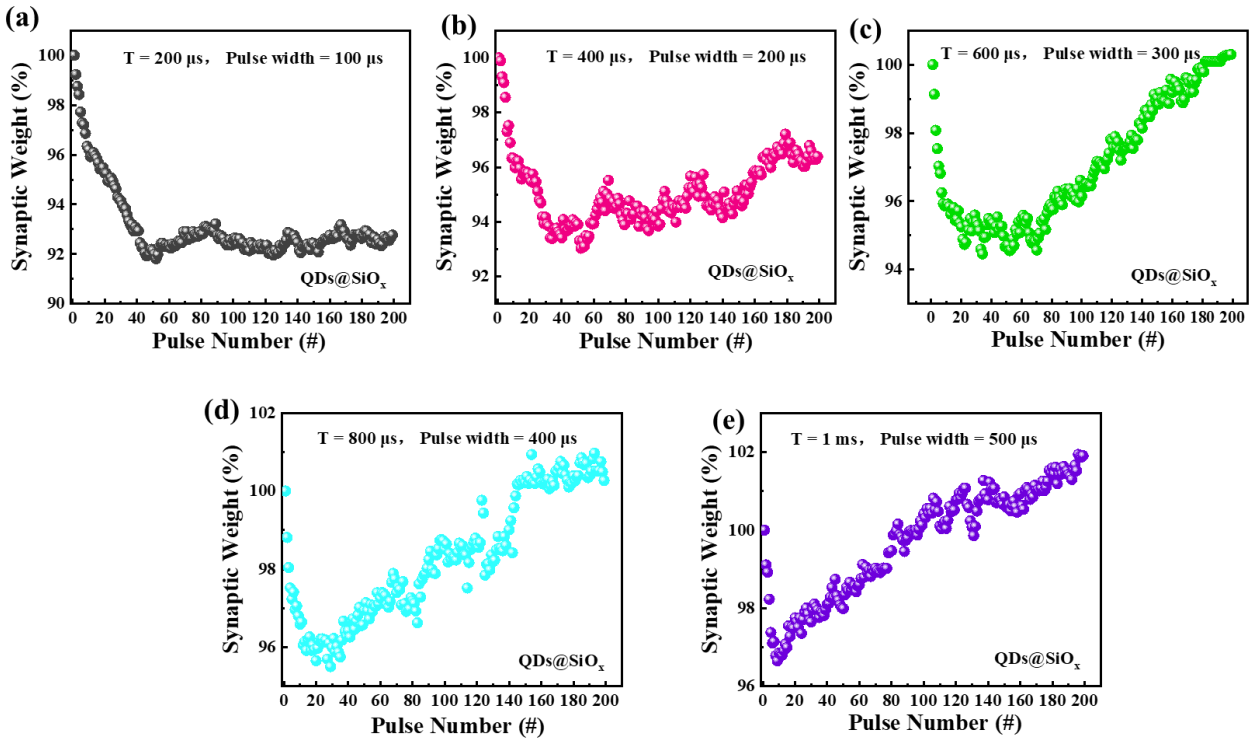

Figure S7. Synaptic weights for different pulse widths: (a) 200 µs, (b) 400 µs, (c) 600 µs, (d) 800 µs, and (e) 1 ms.

8. EPSC behavior of Pt/PLiCoO$_2$/QDs@SiO$_x$/Si

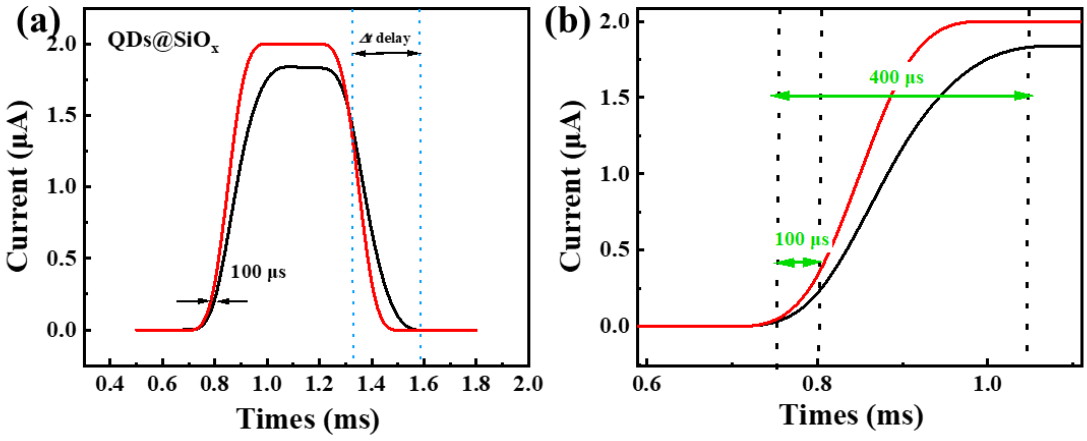

Figure S8. EPSC behavior: (a) The synaptic weight can be dramatically modulated by the pulse interval between the excitatory postsynaptic current (EPSC) and spikes. A single synaptic spike (5 V, 1 ms) can trigger EPSC and the intensity declines gradually to zero in a few hundred microseconds after the pulse. It may be because after the pulse voltage is removed, lithium ions can still traverse a short distance due to inertia.[1] (b) The switching speed of the device is measured to be 100 ~ 400 μs.

9. Summary of energy consumption for synaptic memristor

Table S1. Summary of energy consumption for various synaptic memristor such as oxide, two dimensional materials and perovskite.

Structure	Energy consumption	Refs.
2D MoS_2/Nb_2O_5	~6 pJ	[2]
HfO_y/HfO_x	30 pJ	[3]
$Zr_{0.5}Hf_{0.5}O_2$:Gr-QDs	8 pJ	[4]
ZnO/Ta_2O_5	35 pJ	[5]
Bi:SnO_2	28 pJ	[6]
Ta_2O_5	82.4 pJ ~162 pJ	[7]
Ag-Au/SiO_x	75 pJ~207 pJ	[8]
TiO_2:Ag	26 pJ	[9]
$HfSe_xO_y/HfSe_2$	0.1 fJ~0.1 pJ	[10]
MgO/Mg/MgO	560 pJ	[11]
SiO_x/Graphene/SiO_2	2 pJ	[12]
Ti/TiO_2/Nb:STO	4.1 pJ	[13]
BiOI	0.1 pJ	[14]
P$LiCoO_2$/QDs@SiO_2	650 pJ~2.6 nJ	Our results

10. Preparation of QDs@SiO_x/Si

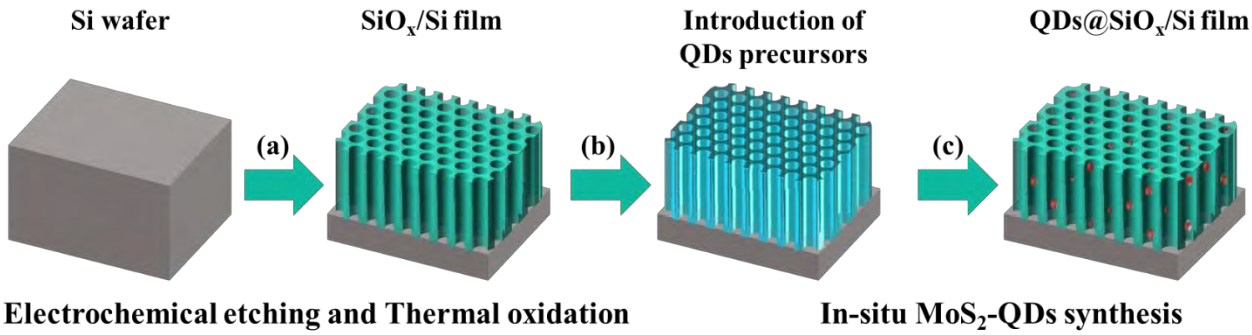

Figure S9. (a)-(c) Fabrication process of the SiO_x/Si film by electrochemical etching and thermal oxidation.

References

[1] Wang, Z. Q., Xu, H. Y., Li, X. H., Yu, H., Liu, Y. C., Zhu, X. J. Synaptic learning and memory functions achieved using oxygen ion migration/diffusion in an amorphous InGaZnO memristor. Adv. Funct. Mater. 22 (2012) 2759-2765.

[2] J. H. Nam, S. Oh, H. Y. Jang, O. Kwon, H. Park, W. Park, J. D. Kwon, Y. Kim, B. Cho, Adv. Funct. Mater. 31 (2021) 2104174.

[3] J. Yin, F. Zeng, Q. Wan, F. Li, Y. Sun, Y. Hu, J. Liu, G. Li, F. Pan, Adv. Funct. Mater. 28 (2018) 1706927.

[4] X. Yan, L. Zhang, H. Chen, X. Li, J. Wang, Q. Liu, C. Lu, J. Chen, H. Wu, P. Zhou, Adv. Funct. Mater. 28 (2018) 1803728.

[5] P. Balakrishna Pillai, M. M. De Souza, ACS Appl. Mater. Inter. 2017, 9, 1609-1618.

[6] Y. Liu, C. Ye, K. C. Chang, L. Li, B. Jiang, C. Xia, L. Liu, X. Zhang, X. Liu, T. Xia, Z. Peng, G. Cao, G. Cheng, S. Ke, J. Wang, Small 16 (2020) 2004619.

[7] M. Kim, M. A. Rehman, D. Lee, Y. Wang, D. Lim, M. F. Khan, H. Choi, Q. Y. Shao, J. Suh, H. Lee, H. Park, ACS Appl. Mater. Inter. 14 (2022) 44561-44571.

[8] Z. Ma, J. Ge, W. Chen, X. Cao, S. Diao, Z. Liu, S. Pan, ACS Appl. Mater. Inter. 14 (2022) 21207-21216

[9] X. Yan, J. Zhao, S. Liu, Z. Zhou, Q. Liu, J. Chen, X. Y. Liu, Adv. Funct. Mater. 28 (2018) 1705320.

[10] L. Liu, Y. Li, X. Huang, J. Chen, Z. Yang, K. H. Xue, M. Xu, H. Chen, P. Zhou, X. Miao, Adv. Sci. 8 (2021) 2005038.

[11] B. Dang, Q. Wu, J. Sun, M. Zhao, S. Wang, F. Song, M. Yang, X. Ma, H. Wang, Y. Hao, IEEE Electr. Device L. 40 (2019) 1265-1258.

[12] S. Choi, J. Choi, J. C. Kim, H. Y. Jeong, J. Shin, S. Jang, S. Ham, N. D. Kim, G. Wang, Nano Energy 84 (2021) 105947.

[13] N. Yang, J. Zhang, J. Huang, Y. Liu, J. Shi, Q. Si, J. Yang, S. Li, ACS Appl. Electron. Mater. 4 (2022) 3154-3165.

[14] P. Lei, H. Duan, L. Qin, X. Wei, R. Tao, Z. Wang, F. Guo, M. Song, W. Jie, J. Hao, Adv.

Funct. Mater. 32 (2022) 2201276.